Oxygen Dynamics in Transition Metal Doped Bismuth Oxides

Julia Wind[1†*], Richard A. Mole[2] and Chris D. Ling[1]

[1]*School of Chemistry, The University of Sydney, Sydney 2006, Australia*
[2]*Australian Centre for Neutron Scattering, ANSTO, New Illawarra Road, Lucas Heights 2234, Australia*
[†]*Current Address: Department of Chemistry, University of Oslo, Blindern, P.O. Box 1033, 0315 Oslo, Norway*

Abstract

A detailed quasielastic neutron scattering (QENS) study provides direct insights into the mechanism of ionic conduction in the Type II transition metal-doped bismuth oxides $Bi_{22}W_5O_{48}$, $Bi_{22}Nb_5O_{45.5}$ and $Bi_{22}W_{2.5}Nb_{2.5}O_{46.75}$. Quantitative analysis of the QENS broadening reveals an oscillating behavior similar to that observed recently for pure fluorite-type δ-Bi_2O_3, which can be adequately modeled by a coherent adaption of the Chudley-Elliot jump diffusion model. In conjunction with detailed *ab initio* molecular dynamics simulations, this shows that oxygen diffuses through these compounds almost exclusively within fluorite-type regions *via* an isotropic, liquid-like mechanism. The average oxygen jump length is slightly shorter than half the length of the fluorite-type subcell; this is attributed to the flexible coordination environments around Bi, in contrast to the more regular coordination environments around the transition metal dopants, which localize vacancies and prevent the remaining oxygen atoms from contributing to the overall oxygen diffusivity.

1. Introduction

A deep understanding of solid-state ionic conductors, sufficient to rationally modify existing materials and design new ones with improved performance, entails a detailed knowledge of their atomic-scale structures and dynamics. Quasielastic neutron scattering (QENS) is a particularly powerful method for this purpose, because it simultaneously probes the diffusive properties (in the QENS signal) and the lattice dynamics (in the form of the generalized density of states, GDOS).

The quantity measured in a QENS experiment is the dynamic scattering function $S(Q,\omega)$, where Q is the momentum transfer (in $Å^{-1}$) and ω the energy transfer (in meV). $S(Q,\omega)$ includes coherent and incoherent contributions, arising from the pair- and self-correlated effects respectively. The dynamical scattering functions are directly related to the van Hove[1] correlation

functions G(r,t) and $G_s(r,t)$. The coherent scattering function $S_{coh}(Q,\omega)$ is the double Fourier transform in space and time of the time-dependent pair-correlation function G(r,t) which gives the probability that, given an atom at the origin at time $t = 0$, the same or any other atom will be located at a position r at time t. The incoherent scattering function $S_{inc}(Q,\omega)$ is the double Fourier transform of the time-dependent self-correlation function $G_s(r,t)$ which gives the probability of finding the same particle at a position r from its original position at time t.

Because self-correlation is simpler and more directly applicable to the diffusion of an ion through an otherwise ordered crystal lattice, a number of well-tested models have been developed to analyze incoherent scattering. Consequently, the overwhelming majority of ionic conductors investigated by QENS are proton conductors, because hydrogen has a very large and almost purely incoherent scattering cross section.[2-5] Recent interest in solid-state battery materials (in particular) has inspired a growing number of QENS studies of mixed coherent and incoherent scatterers such as Li[6-9] and Na;[10] however, the analysis still always focuses on the incoherent part of the scattering function due to the lack of suitable models for dealing with the coherent part.

We recently addressed this in a QENS investigation of diffusion behavior of an almost purely coherent scatterer, O.[11] We chose δ-Bi_2O_3 as our model system due to its small unit cell, the presence of only two atomic species, and its extremely high oxide-ionic conductivity. We applied Sköld's modification to solid-state conduction for the first time, successfully extending methods that had previously only been applied to liquids. The resulting analysis revealed an isotropic jump diffusion process with a distribution of jump lengths.

Although an ideal test system for the reasons noted above, δ-Bi_2O_3 is not a practical material for applications such as fuel-cell membranes, because it is only stable in the very narrow temperature window 729–817 °C, between its transformation from the low-temperature β-phase and its melting point.[12-13] To test and validate our approach in a slightly more complex but potentially more useful system, in the present study we turned to transition metal-doped bismuth oxide. Such doping can introduce complex ordered superstructures while retaining the average fluorite-type δ-Bi_2O_3 substructure, along with good (albeit reduced) oxide-ionic conduction properties. The most attractive for these purposes are the so-called "Type II" incommensurately modulated phases, the structures of which we recently solved in the Bi-Nb-O,[14-15] Bi-W-O[16-17] and mixed Bi-Nb-W-O[18] systems. We initially focused on Type II Bi-W-O because its structure is adequately described in the commensurate approximation by a relatively small 3x3x3

supercell, in which we can just feasibly carry out *ab initio* molecular dynamics (AIMD) simulations to help validate conclusions about the oxide-ion conduction mechanisms in Type II structures, as we did for pure δ-Bi_2O_3.[11] We then extended the experimental part of the study to the Type II Bi-Nb-O and mixed Bi-Nb-W-O systems, the structures of which require larger supercells that are not computationally feasible for AIMD.

2. Experimental Details

Synthesis

Polycrystalline samples of compositions $Bi_{22}W_5O_{48}$, $Bi_{22}Nb_5O_{45.5}$, $Bi_{22}W_{2.5}Nb_{2.5}O_{46.75}$ were synthesised by ball-milling stoichiometric quantities of WO_3 (99.999 %), Nb_2O_5 (99.998 %) and Bi_2O_3 (99.999 %, dried at 600 °C for 5 h). The samples were then placed in open alumina crucibles and heated to 850 °C for 5 h. After thorough regrinding in an agate mortar and pestle, samples were sintered at 1000 °C for another 5 h. Phase-pure samples were then pressed into rods (0.7 cm diameter, 4-6 cm length) and sintered at 950 °C for 5 h. Phase purity of the samples at room temperature was confirmed by powder X-ray diffraction (PXRD) using a Panalytical X'pert Pro diffractometer in Bragg-Brentano geometry with non-monochromated Cu Kα radiation.

Data Collection and Analysis

Inelastic neutron scattering (INS) data were collected on pressed and sintered rods of $Bi_{22}W_5O_{48}$, $Bi_{22}Nb_5O_{45.5}$ and $Bi_{22}W_{2.5}Nb_{2.5}O_{46.75}$ on the cold-neutron time-of-flight spectrometer PELICAN[19-20] at the Australian Centre for Neutron Scattering, ANSTO, using 6 Å and 3 Å incident neutrons. Using a similar setup as for our data collection on δ-Bi_2O_3,[11] sample rods were placed inside a Pt can, hung into the vacuum furnace using Pt wire and covered with a Pt lid. Short data collections of 1 h each were performed on heating at 150, 300, 450, 600 and 750 °C using 6 Å incident neutrons. A long data collection of 12 h was carried out at 950 °C. A 1 h data set using an incident wavelength of 3 Å was collected at 950 °C to check for phases and to extract lattice parameters.

A vanadium standard was measured for detector normalization and to determine the resolution function for the quasielastic neutron scattering (QENS) analysis. The background was corrected by subtracting an empty sample can. The corrected time-of-flight spectra were then converted to $S(Q,\omega)$. All data manipulations were done using the Large Array Manipulation Program (LAMP).[21] For QENS analysis, detectors containing Bragg reflections were removed from the data prior to further data processing. The obtained Q-slices (with a Q-rebin of $dQ = 0.1$ Å^{-1})

were then fit using the QENS_fit program within LAMP. All Q-slices could be adequately fitted using a combination of a δ-function and one Lorentzian peak convoluted with the measured resolution function (vanadium standard) and a small linear sloping background. All fits were done over an energy range of $-1 \leq \omega \leq 1$ meV, chosen to be symmetric around ω = 0.

The generalized density-of states (GDOS) was obtained from S(Q,ω) using the equation

$$G(Q,\omega) = \frac{\omega}{Q^2} S(Q,\omega) \left[1 - exp\left(-\frac{\omega}{k_B T}\right)\right] \quad (1)$$

followed by integration over Q.

Ab Initio Simulations

Ab initio molecular dynamics (AIMD) calculations were performed using density functional theory-based methods as implemented in the Vienna *ab initio* simulation package (VASP).[22-23] The generalized gradient approximation (GGA) in the scheme of PBE (Perdew-Burke-Ernzerhof)[24] was employed. Calculations used projector-augmented wave (PAW) pseudopotentials[25] with a plane wave cut-off energy of 400 eV. Sampling of the electronic structure in reciprocal space was performed at the Γ-point only.

The geometry optimised commensurate approximate structure for $Bi_{22}W_5O_{48}$, presented in our previous work,[17] was used as a starting model for our AIMD simulations. Periodic boundary conditions were used so that O diffusion can occur from one unit cell to the next. Lattice parameters were fixed to the experimental values at the corresponding simulation temperatures.[16-17] AIMD simulations were performed using the canonical ensemble (NVT), where a constant temperature was achieved through a simple velocity-scaling scheme as implemented in VASP. Simulations were performed at room temperature (12 ps) as well as at 1250 K (22 ps), employing a constant time step of 2 fs. The first 2 ps were removed from the trajectory prior to further analysis to allow the system to equilibrate.

Visual inspection of the AIMD trajectories and the calculation of ellipsoids (as shown in Figure 9) was carried out in the Structures Magdraw Atoms Editor in LAMP. Subsequent analysis of the trajectories was done using the program MDANSE[26] (mean square displacement parameters (MSDs), pair distribution functions (PDF), GDOS). Additional Python scripts were written to extract coordination numbers and their variation with simulation time.

3. Results and Discussion

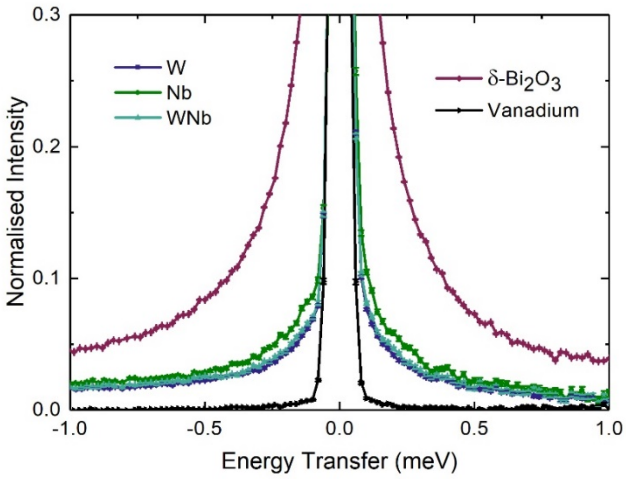

Figure 1: Comparison of the QENS broadening. *Q*-integrated data normalized to the total elastic intensity for $Bi_{22}W_5O_{48}$, $Bi_{22}Nb_5O_{45.5}$, $Bi_{22}W_{2.5}Nb_{2.5}O_{46.75}$, δ-$Bi_2O_3$ (at 730 °C) and the resolution function (vanadium standard), measured using λ = 6 Å.

Figure 1 compares the QENS broadening (*Q*-integrated data normalized to the total elastic intensity) for $Bi_{22}W_5O_{48}$, $Bi_{22}Nb_5O_{45.5}$, $Bi_{22}W_{2.5}Nb_{2.5}O_{46.75}$ (at 950 °C) and δ-Bi_2O_3 (at 730 °C).[11] This shows a clear QENS broadening for all our investigated transition metal-doped samples (compared to the resolution function), although significantly weaker (approximately 1/3 of the total integrated normalised intensity) compared to δ-Bi_2O_3, in agreement with the lower oxygen ionic conductivity.[16]

Oxygen Dynamics in Type II $Bi_{22}W_5O_{48}$

QENS Analysis – Experimental Oxygen Dynamics.

Figure 2 shows the temperature dependence of neutron scattering data collected on PELICAN at an incident neutron wavelength of λ = 6 Å. The temperature dependence of the elastic scattering data (elastic diffraction patterns, S(*Q*, ω = 0)) is shown in Figure 2a. The Bragg peaks observed at lower temperature (150-600 °C) are superstructure peaks due to Type II-like ordering within the oxygen sublattice, and thus confirm the presence of Type II Bi-W-O within that temperature range. In agreement with our recent *in situ* NPD study,[16] a decomposition and phase transition to the thermodynamically stable combination of Type Ib + Aurivillius phases is observed at around 750 °C. At 950 °C, the sample transforms back to single-phase Type II.

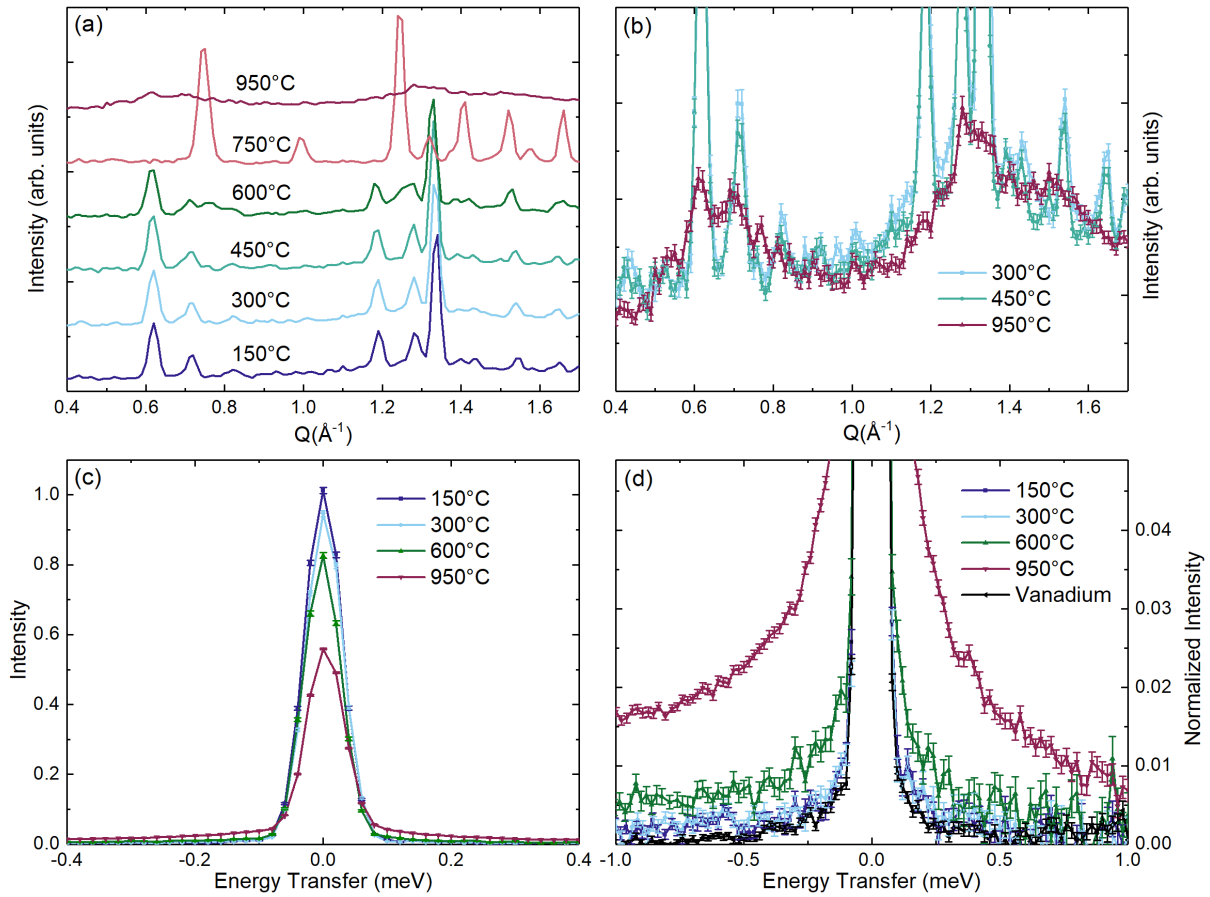

Figure 2: Temperature dependence of INS data for $Bi_{22}W_5O_{48}$. (a) Elastic line; (b) zoom into background of the elastic line; (c) total Q data, showing a decrease in elastic intensity and (d) total Q data normalized to the total elastic intensity showing the increase in QENS broadening.

The significant decrease in intensity of the superstructure peaks (which almost disappear within the two broad diffuse peaks, see Figure 2b) is a clear indication of an increase in oxygen disorder in the sample compared to the quenched low-temperature type II phase. Note the clear structure in the background of the elastic line for the Type II phase, with two broad peaks centred at $Q \approx 0.7$ and $Q \approx 1.3$ Å^{-1}. We observed similar diffuse peaks in the elastic diffraction patterns for pure δ-Bi_2O_3.[11]

Figure 3 shows the dynamic scattering function $S(Q,\omega)$ for $Bi_{22}W_5O_{48}$ at 950 °C. A clear QENS broadening is observed over the entire Q-range. The well-defined streak into the inelastic region at high Q is a phonon emerging from the ⟨111⟩ Bragg reflection just outside the experimentally accessible Q-range at $Q = 2.0$ Å^{-1}.

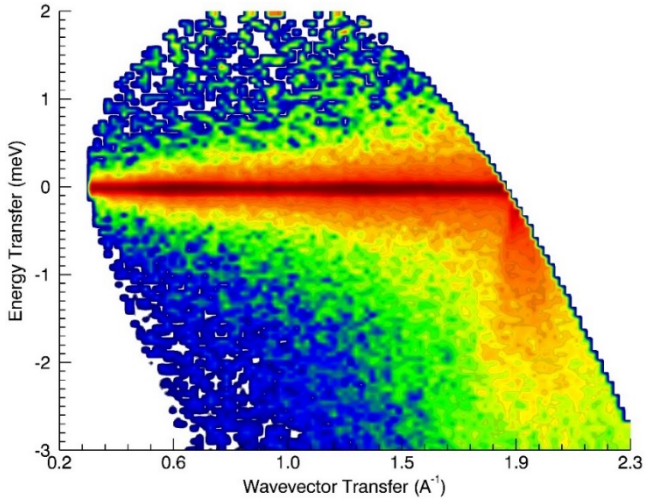

Figure 3: Dynamic scattering function S(Q,ω) for W-doped Bi_2O_3 at 950 °C measured at λ = 6 Å, showing clear QENS broadening as well as a pronounced structure along the elastic line (ω = 0). Impurity Bragg reflections have not been removed for this figure.

To obtain further insights into the oxygen dynamics in the sample, the Q-dependence of the QENS signal was analysed. The apparent variation in QENS broadening with Q is a clear indication for translational diffusion in the sample. Constant-Q slices (dQ = 0.1 Å^{-1}) were fit with a combination of one δ-function (elastic contributions) and one Lorentzian (quasielastic contributions) peak, convoluted with the experimental resolution function (vanadium standard) and a linear sloping background.

The extracted Lorentzian HWHM as a function of Q are shown in Figure 4a. Fitting of a conventional incoherent Chudley-Elliot[27] (iCE) jump diffusion model, given by

$$\Delta\omega(Q) = \frac{1}{\tau}\left(1 - \frac{\sin(Qd)}{Qd}\right) \qquad (2)$$

(where τ is the residence time of the diffusing species on a given site and d is the jump distance), against the data yields a jump distance of d = 4.8(2) Å and a residence time of τ = 5.8(2) meV^{-1} (dashed black line Figure 4a). However, the iCE model clearly fails to reproduce the oscillating behavior of the QENS broadening. Closer inspection of the QENS broadening reveals de Gennes narrowing,[28] i.e., the quasielastic (Lorentzian) line width narrows when the elastic structure factor (Figure 4b) reaches is maximum. This must be considered when modeling the QENS data. Following our previously reported approach for δ-Bi_2O_3,[11] we account for coherency effects in the sample by applying Sköld's *ad hoc* modification[29] to the iCE model to obtain the modified coherent Chudley-Elliot (cCE) model, given by

$$\Delta\omega(Q) = \frac{1}{\tau S(Q)}\left(1 - \frac{\sin(Qd)}{Qd}\right) \qquad (3)$$

where S(Q) is the total structure factor obtained by integrating over all energy transfers. The limited accessible Q range and the presence of Bragg peaks prevents a reliable determination of S(Q) in absolute units. For the following analysis, S(Q) was assumed to approach 1 at the highest measured Q value, just below the first Bragg peak. Note that due to the direct correlation with the normalization of S(Q), residence times τ (and consequently diffusion coefficients) can only be roughly estimated.

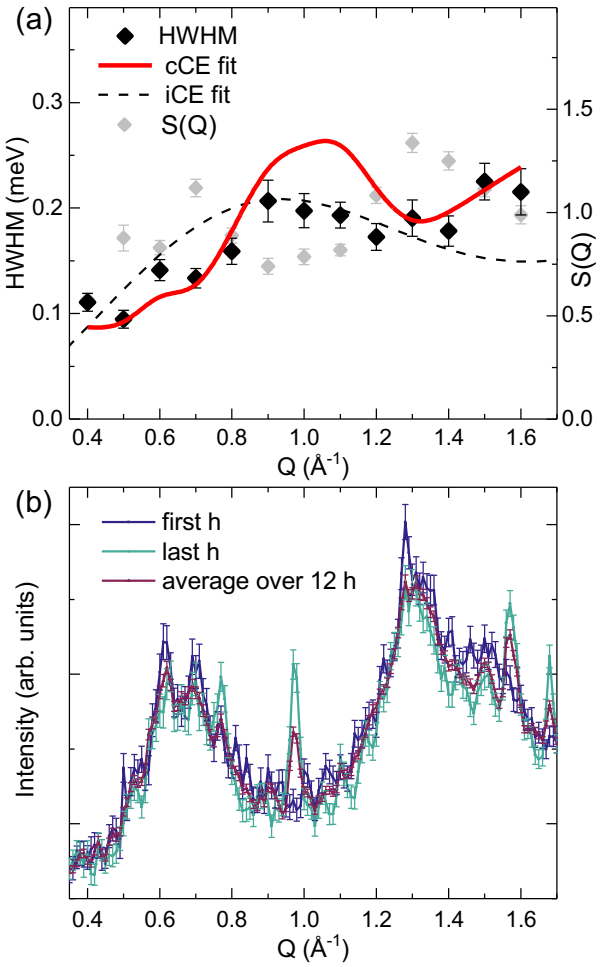

Figure 4: (a) Q-dependence of the QENS signal for $Bi_{22}W_5O_{48}$ at 950 °C (black diamonds). The red line shows a cCE fit, the black dashed line a fit using a conventional iCE. (b) Extraction of the elastic line after 1 h of data collection (green) and after 12 h (blue) of data collection, showing the appearance of two Bragg peaks at Q-values of 0.97 and 1.57 Å^{-1} respectively. The red line shows the average over 12 h collection time.

The cCE fit against HWHM data for Type II $Bi_{22}W_5O_{48}$ at 950 °C (red line line in Figure 4a) provides a better description of the oscillating behavior of the QENS broadening. The cCE fit yields a jump length of $d = 3.2(1)$ Å (and a corresponding residence time estimate of $\tau = 5.3(2)$ meV^{-1}). As we found for δ-Bi_2O_3, this value does not correspond to any discrete distance between oxygen sites within the long-range-average crystal structure and is slightly larger than half a fluorite-type subcell (a = 5.628(4) Å, extracted from Rietveld refinement against energy integrated λ = 3 Å data at 950 °C). The similar Q-dependence of the QENS signal

and extracted jump length imply very similar mechanisms of oxygen diffusion in $Bi_{22}W_5O_{48}$ and δ-Bi_2O_3.

Finally, we note the appearance of additional Bragg peaks during the 12 h of data collection at 950 °C (see Figure 4b). These correspond to the formation of small amounts of the Aurivillius-type phase Bi_2WO_6 (confirmed by lab-PXRD after the measurement) on the sample surface due to evaporation of Bi. A thorough time-dependent analysis of the spectra confirmed that the Aurivillius phase made no dynamic contributions to the total signal. Individual Q-spectra containing Aurivillius Bragg peaks were removed prior to analysis. This process also reduced the quality of the data around $Q = 1$ Å^{-1} and explains the discrepancy (lower intensity) in the cCE fit in this Q-range.

To obtain a clearer picture on the atomic-scale diffusion process in $Bi_{22}W_5O_{48}$ and understand the influence of dopants on the diffusion mechanism, we carried out AIMD simulations as described in the next section.

AIMD Analysis

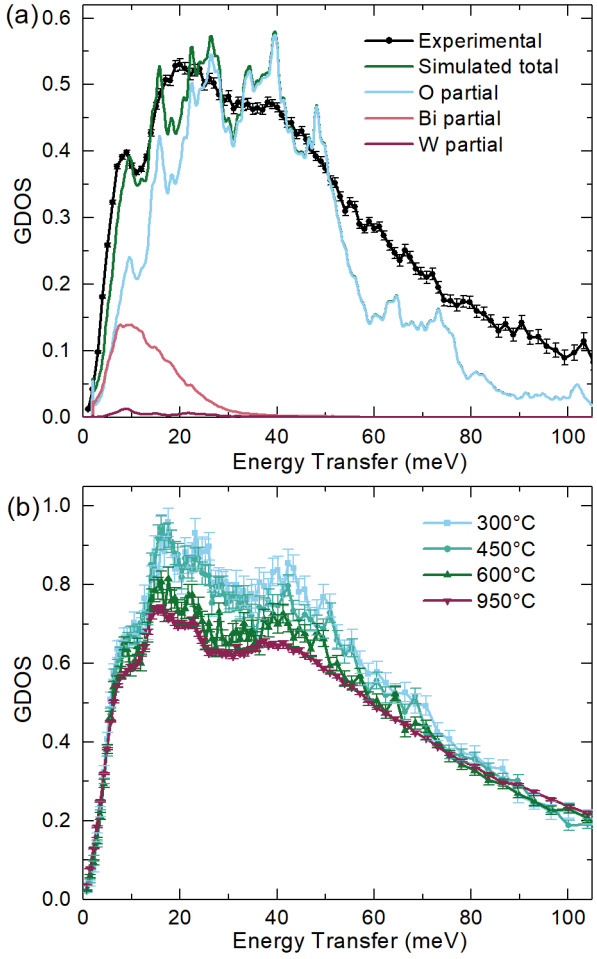

Figure 5: (a) Simulated *vs.* experimental GDOS for $Bi_{22}W_5O_{48}$ measured at room temperature using 4.7 Å neutrons. (b) Temperature dependence of the GDOS measured at 6 Å.

The experimental GDOS measured at room temperature with 4.7 Å neutrons is shown in

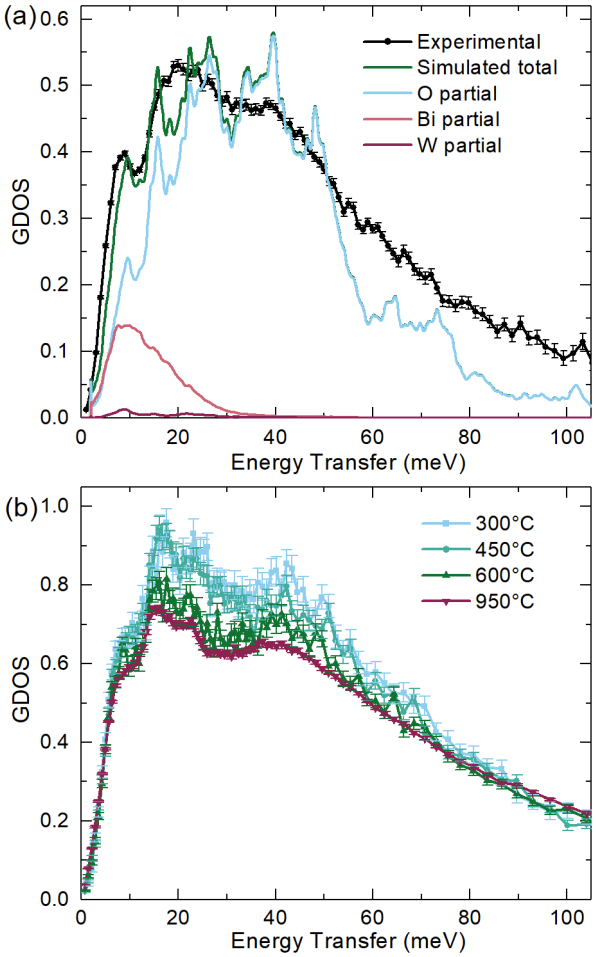

Figure 5a. These data are compared to the simulated GDOS as extracted from AIMD trajectories, showing excellent agreement. The partials are weighted by their neutron scattering cross-sections and number of atoms per formula unit. At low energy transfers, the metal atoms (mainly Bi) contribute to the GDOS, while at higher energy transfers the contributions of oxygens dominate. Due to the low levels of W-doping in the sample and its relatively low scattering cross

section, the contributions to the total GDOS from W are negligible (

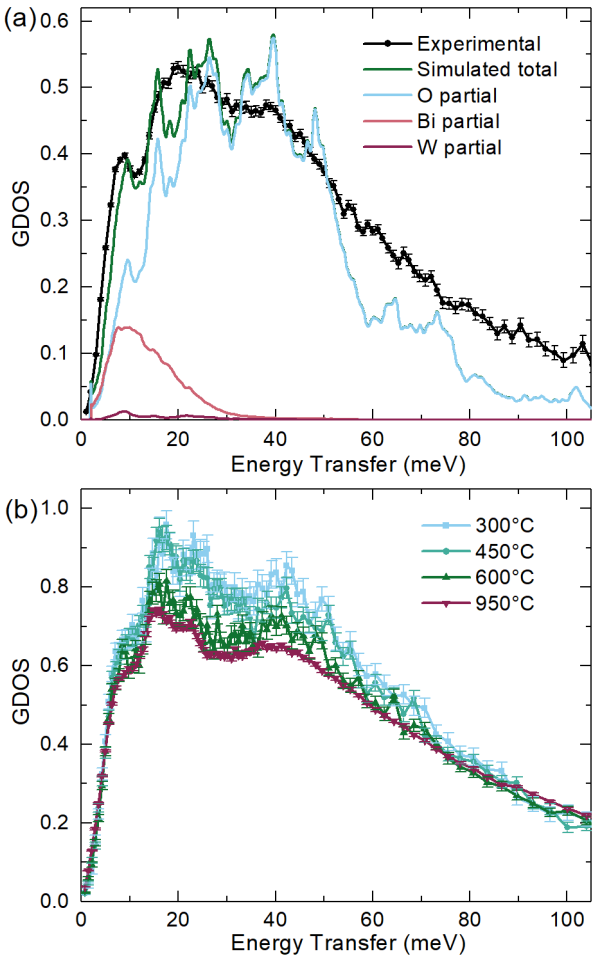

Figure 5b). As expected, the GDOS does not change significantly with temperature. Differences around 20 meV arise from empty can subtractions (metal GDOS shows significant intensities in that area). The GDOS shows slightly more features compared to pure δ-Bi_2O_3. In fact, it looks very similar to δ-Bi_2O_3, for which the peak at ~7.5 meV was also observed. This is consistent with the long-range-ordered oxygen sublattice of the Type II phase compared to the disordered oxygen vacancy distribution in δ-Bi_2O_3.

The pair distribution function (PDF) extracted from the AIMD simulation at 977 °C (1250 K) is

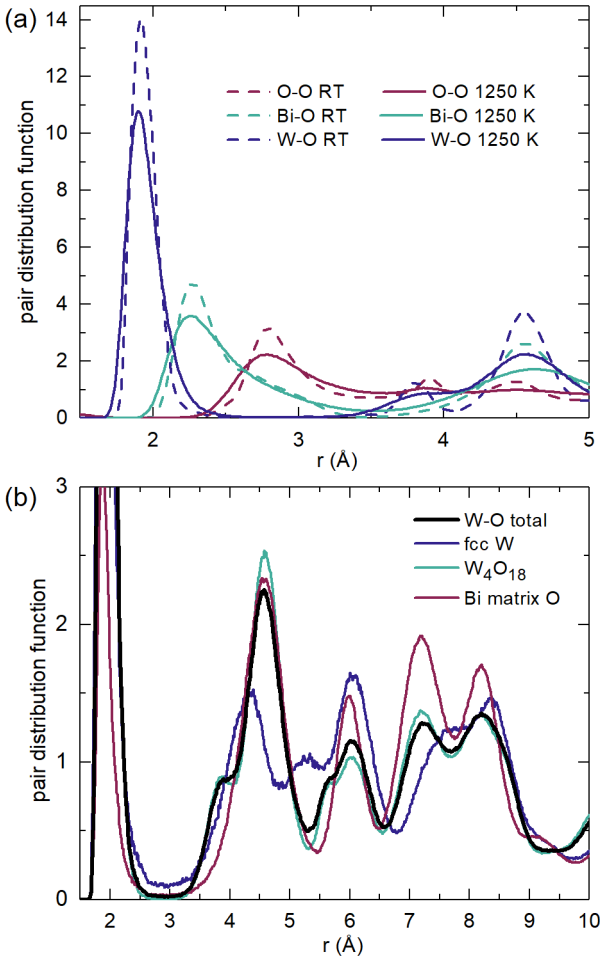

presented in

Figure 6 and shows clear differences between Bi and W. The PDF for W-O is much narrower, indicating more regular coordination environments compared to the broader Bi-O peaks in the PDF. The main peak in $PDF_{W\text{-}O}$ is located at smaller distances compared to $PDF_{Bi\text{-}O}$, in agreement with the difference in ionic radii ($r(Bi^{3+})$ = 1.7 Å, $r(W^{6+})$ = 0.74 Å[30]). The PDF for oxygen, $PDF_{O\text{-}O}$, is almost featureless above 4 Å, indicative of oxygen disorder. The PDF for atoms located in W_4O_{18} clusters shows slightly narrower and better-defined peaks, while contributions from oxygen atoms within the Bi matrix cause peaks to broaden.

No significant differences were observed between the PDFs for W4 and W5 compositions. At room temperature, the PDF peaks are generally better defined. For Bi, it appears that the first peak splits into two, with maxima at 2.27 Å and 2.66 Å, suggesting two different coordination spheres of 2.2-2.4 Å and 2.4-3.1 Å respectively.

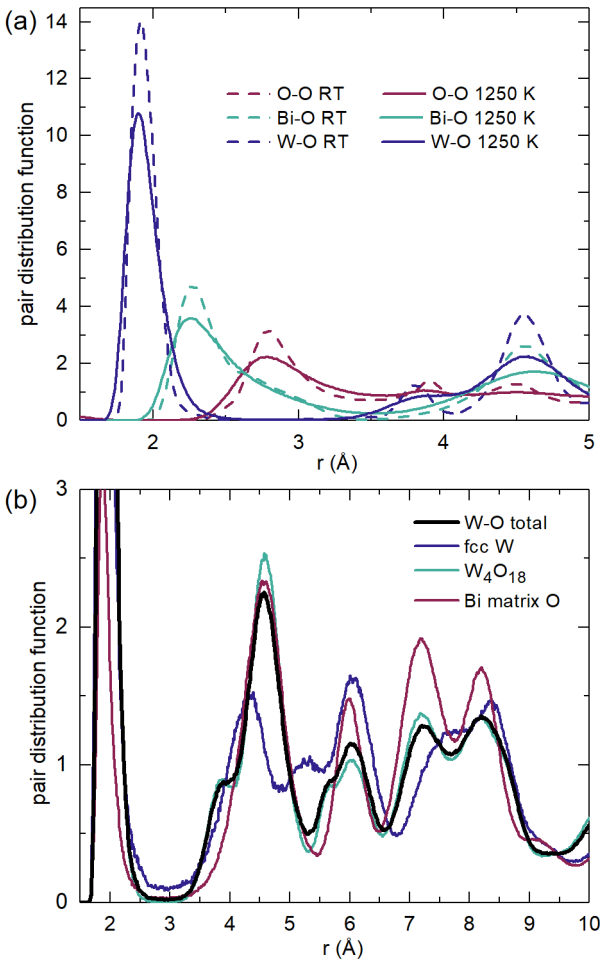

Figure 6: Pair distribution functions (PDF) for $Bi_{22}W_5O_{48}$ extracted from AIMD simulations. (a) Comparison between room temperature (dashed lines) and 977 °C (solid lines). (b) Partial PDFs for W-O in different structural environments.

Averaged coordination numbers (CN) were obtained by integrating the PDF up to the first minimum (d_{max} = 2.8 Å was used as a cut-off for W coordination spheres, d_{max} = 3.5 Å for Bi).

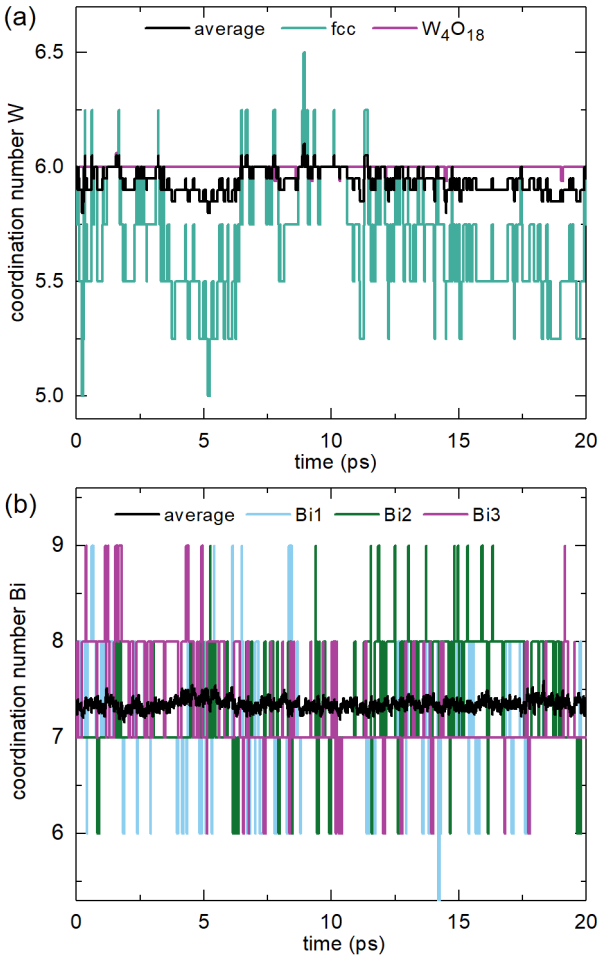

Figure 7a shows the average CN for W as a function of simulation time. The CN was found to be almost exactly 6 for W in W_4O_{18} units, and slightly lower than 6 for W atoms at the fcc position. This is in perfect agreement with previous XANES results that revealed octahedral W coordination throughout the entire type II Bi_6WO_{12} solid-solution range.[16]

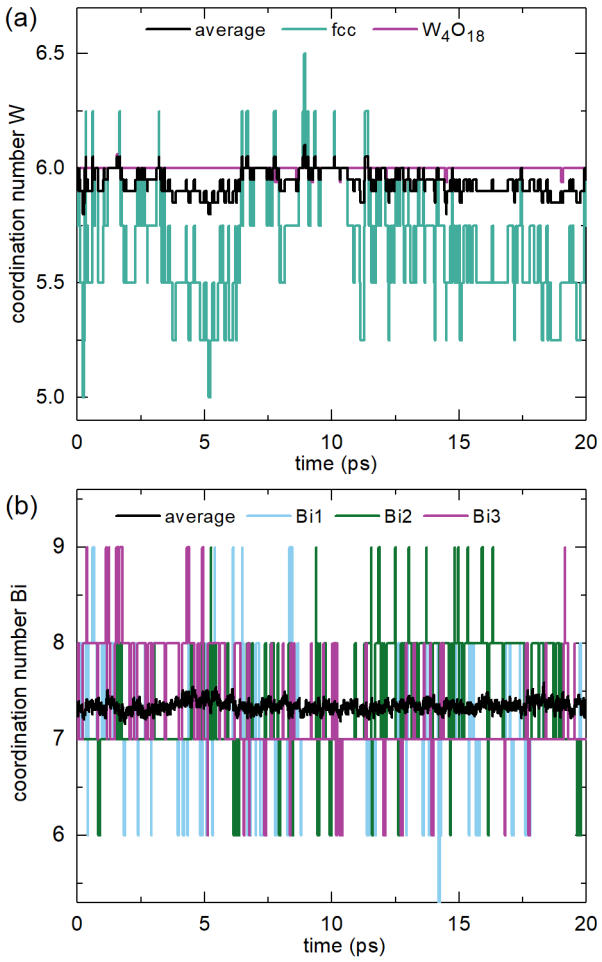

The average coordination of Bi (black line in Figure 7b) was found to be significantly higher, adopting an average value of 7.4. Bi coordination also shows much higher fluctuations as illustrated by the plot of the CN variation

for three selected individual Bi atoms (green, blue and purple lines in

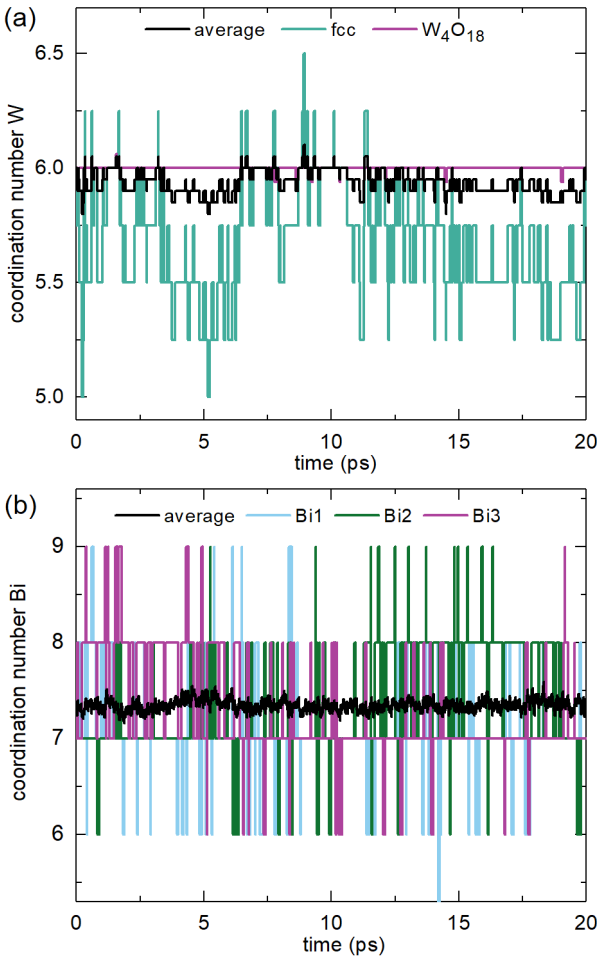

Figure 7b). The ability of Bi to adapt a large variety of different coordination environments clearly plays a crucial role in the oxygen diffusion process.

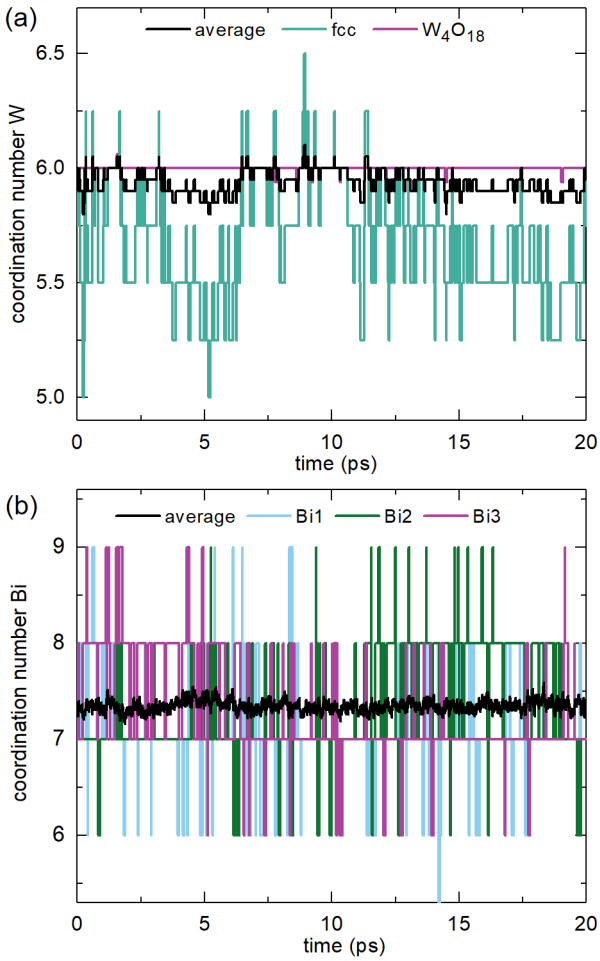

Figure 7: Variation of the coordination numbers for (a) Bi and (b) W over the course of the simulation.

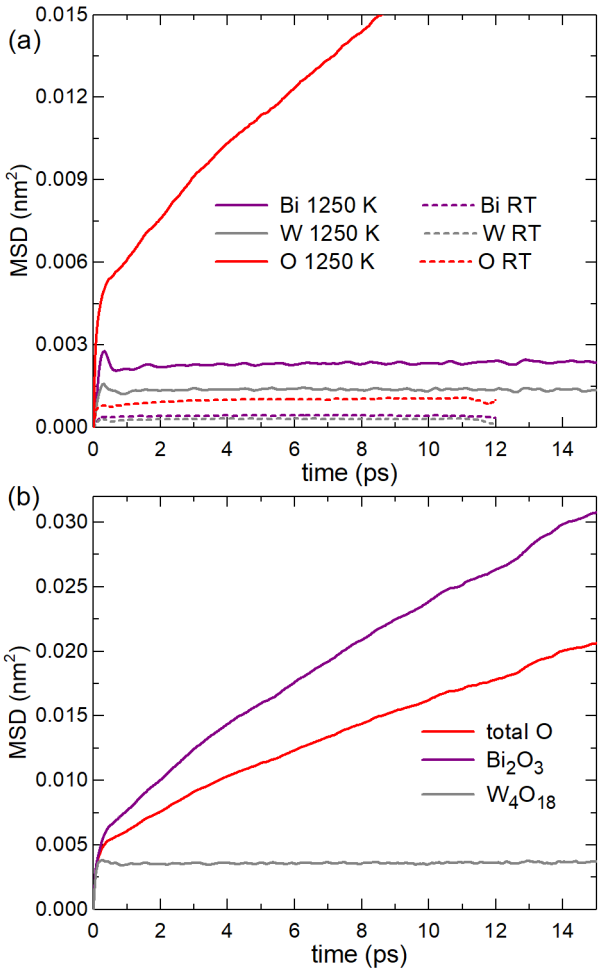

MSDs are shown in

Figure 8a. MSDs for metal atoms (W and Bi atoms), as well as oxygen MSDs for oxygen at room temperature, saturate at low values, corresponding to thermal vibrations around equilibrium positions. At the simulation temperature of 977 °C, oxygen MSDs increase over all simulated time intervals, indicating unrestricted diffusive behavior. A closer inspection of partial MSDs for oxygens in different structural environments (Figure 8b) confirms the well-defined and structurally stable W_4O_{18} tetrahedra of octahedra (no oxygen movement besides thermal vibrations) and diffusive motions of oxygens that are part of the disordered Bi_2O_3-type matrix. This is consistent with a strong preference of W in W_4O_{18} environments for 6-fold coordination (also observed in PDF and coordination number analysis as well as XANES results presented[16]). Oxygen vacancies accumulate around these W atoms to reduce the coordination number, and thus reduce the number of mobile vacancies in the bismuth oxide matrix compared to the pure δ-phase. This also reduces long-range oxygen diffusion in the system.

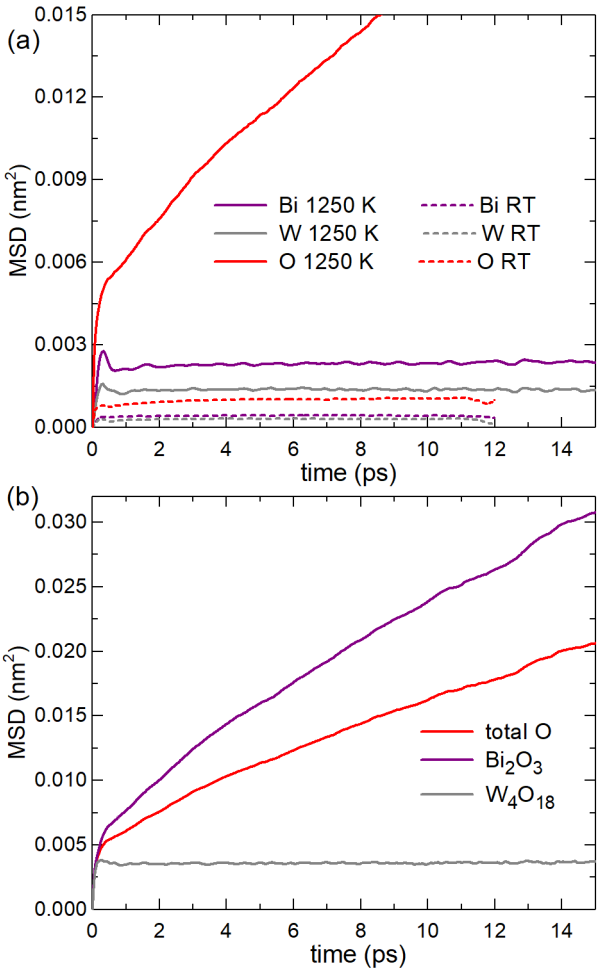

Figure 8: (a) MSDs from simulations at room temperature (dashed) and 977 °C (solid lines); (b) partial MSDs for different O types within the structure.

Figure 9 further illustrates the influence of the dopants on oxygen diffusion behavior within the structure by highlighting the volumes occupied by oxygen ions during the simulations: (a) shows the localised motion of oxygen atoms that are part of W_4O_{18} clusters, while (b) shows the delocalised motion of oxygen atoms within the δ-Bi_2O_3 matrix.

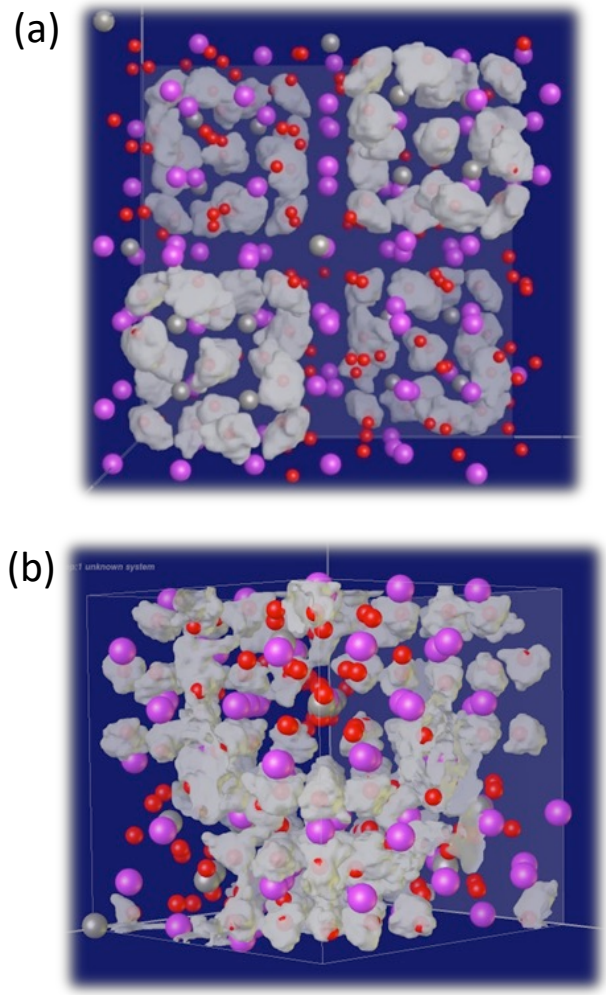

Figure 9: Grey ellipsoids show the volumes explored by oxygen atoms that are (a) part of W_4O_{18} tetrahedra of octahedra, showing localised motion only, and (b) other oxygens, showing diffusive motion.

Dynamics of Other Transition Metal Doped Bismuth Oxides: $Bi_{22}W_{2.5}Nb_{2.5}O_{46.75}$ and $Bi_{22}Nb_5O_{45.5}$

The dynamic scattering functions of Nb-doped and mixed Nb/W-doped samples ($Bi_{22}Nb_5O_{45.5}$ and $Bi_{22}W_{2.5}Nb_{2.5}O_{46.75}$ respectively) at 950 °C are shown in Figure 10. They showed very similar extents of QENS broadening to $Bi_{22}W_5O_{48}$ (cf. Figure 1), suggesting similar dynamics. Both samples show pronounced structure along the elastic line. At temperatures <750 °C, the static structure factor exhibits the characteristic Type II superstructure reflections, which disappear at higher temperatures due to increasing disorder in the oxygen sublattice (Figure 11a). Over the entire temperature range, the background contains two broad peaks centred at $Q \approx 0.7$ Å^{-1} and $Q \approx 1.3$ Å^{-1} respectively.

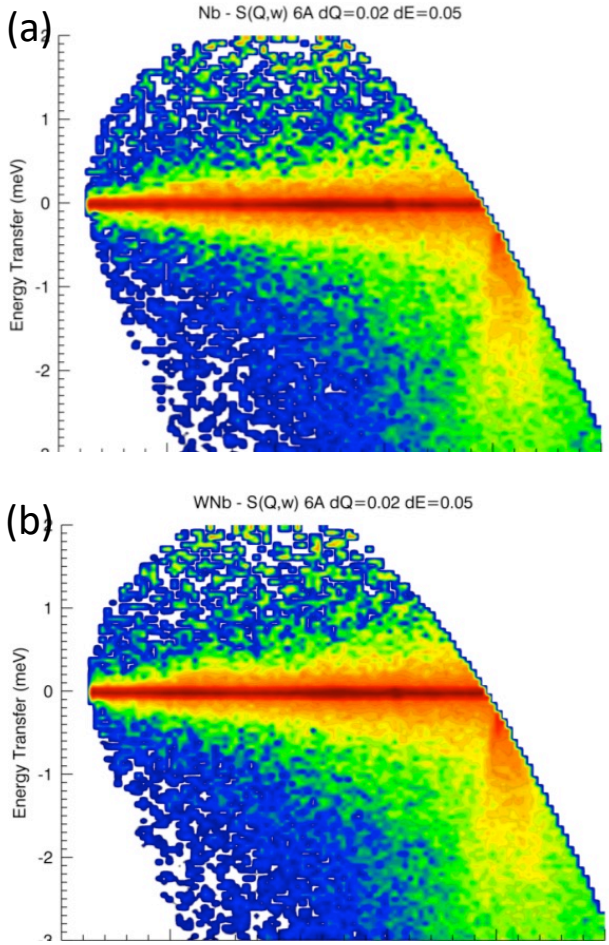

Figure 10: Dynamic scattering function S(Q,ω) for $Bi_{22}Nb_5O_{45.5}$ and $Bi_{22}W_{2.5}Nb_{2.5}O_{46.75}$ at 950 °C measured at λ = 6 Å, both showing a clear QENS broadening and pronounced structure along the elastic line (ω = 0).

Plots of S(ω) (*Q*-integrated data) against energy transfer at selected temperatures for

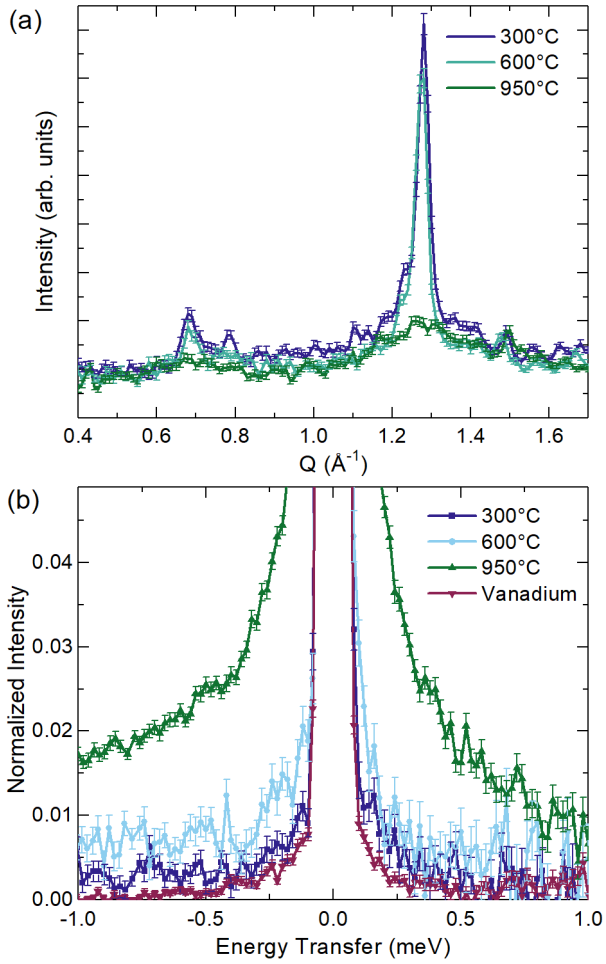

$Bi_{22}W_{2.5}Nb_{2.5}O_{46.75}$ (

Figure 11b) show clear quasielastic broadening, which evolves with temperature due to the continued increase in the rate of oxygen motion in the sample. Constant-*Q* slices through S(*Q*,ω) could be adequately fit using a δ-peak representing the elastic peak and one Lorentzian for quasielastic contributions, convoluted with vanadium as the experimental *Q*-dependent

resolution function. A linear sloping background was included.

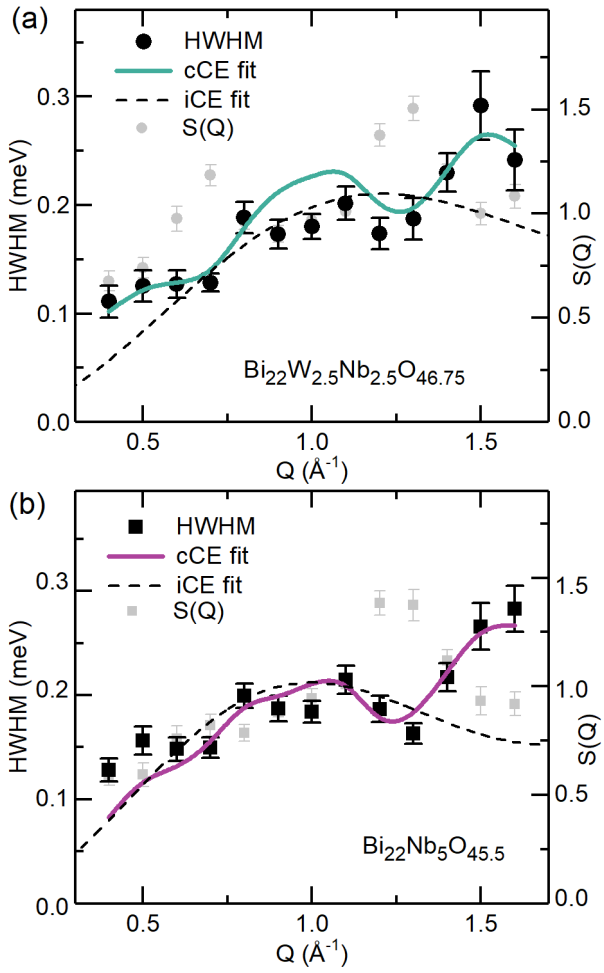

Figure 12 shows the *Q*-dependence of the extracted HWHM and the structure factor S(*Q*). A narrowing of the HWHM at structure factor maxima (de Gennes narrowing), characteristic of coherent scatterers, is apparent. The data were well-fit by a cCE model. The extracted jump distances and corresponding lattice parameters at 950 °C are summarised in Table 1. Lattice parameters were extracted from Rietveld refinements against *Q*-integrated 3 Å data.

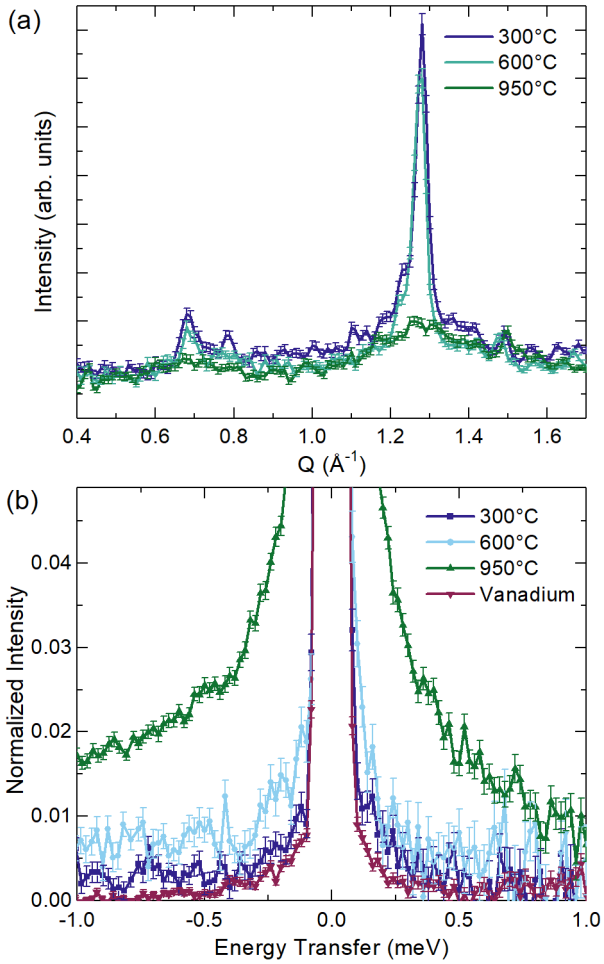

Figure 11: Temperature dependence of INS data for $Bi_{22}W_{2.5}Nb_{2.5}O_{46.75}$: (a) elastic line S($Q$, ω = 0) and (b) QENS broadening (normalised total Q data).

Table 1: Summary of lattice parameter and extracted jump lengths from cCE fits for bismuth oxide-based samples.

Composition	**Lattice parameter *a*/Å**	**Jump distance *d*/Å**
$Bi_{22}W_5O_{48}$	5.628(4)	3.2(1)
$Bi_{22}Nb_5O_{45.5}$	5.576(2)	3.0(1)
$Bi_{22}W_{2.5}Nb_{2.5}O_{46.75}$	5.609(2)	3.0(1)
δ-Bi_2O_3 [11]	5.66	3.33

For all samples, jump lengths slightly larger than half a fluorite-type unit cell length $a_F/2$ were obtained. These suggest that the atomic-scale diffusion mechanisms are very similar to those proposed for $Bi_{22}W_5O_{48}$ in the previous section. Introducing dopants leads to the localisation of oxygen atoms (and vacancies) around the dopants, and oxygen diffusion in the structure occurs *via* an isotropic jump-diffusion process within the δ-Bi_2O_3-type matrix. This results in a slightly reduced average isotropic jump distance relative to $a_F/2$ in the doped samples compared to pure

δ-Bi_2O_3. The differences in total integrated normalised intensity (cf. Figure 1) can be explained by looking at the total vacancy concentration in the samples, which decreases with increasing oxidation state of the dopant atoms (δ-Bi_2O_3 > $Bi_{22}Nb_5O_{45.5}$ > $Bi_{22}W_{2.5}Nb_{2.5}O_{46.75}$ > $Bi_{22}W_5O_{48}$).

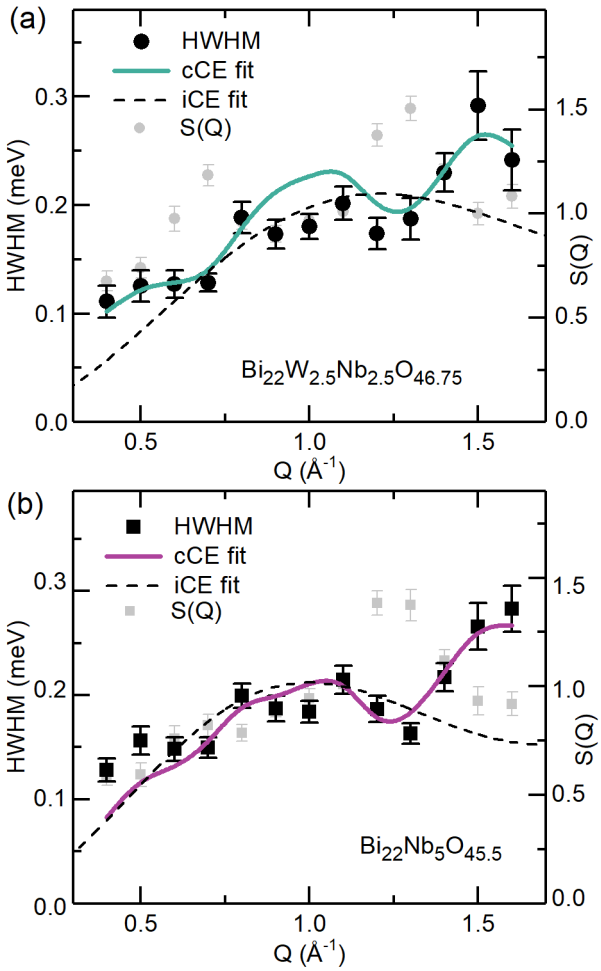

Figure 12: *Q*-dependence of the QENS signal at 950 °C for (a) $Bi_{22}W_{2.5}Nb_{2.5}O_{46.75}$ (black circles) and (b) $Bi_{22}Nb_5O_{45.5}$ (black squares). Solid coloured lines show cCE fits, dashed lines a conventional iCE fit. Grey symbols show the normalised structure factor S(*Q*), illustrating de Gennes narrowing.

4. Conclusions

We have successfully applied our previously developed adaptation for the analysis of coherent QENS data on the example of the very simple model system δ-Bi_2O_3 [11] to the structurally more complicated, but also more stable oxygen ionic conductors $Bi_{22}W_5O_{48}$, $Bi_{22}Nb_5O_{45.5}$ and $Bi_{22}W_{2.5}Nb_{2.5}O_{46.75}$.

The extracted jump lengths obtained by fitting a coherent adaption of the Chudley-Elliot jump diffusion (cCE) model in all investigated samples were found to be slightly larger than $a_F/2$ of the fluorite-type subcell. This is qualitatively the same result as we obtained for pure δ-Bi_2O_3, implying similar mechanistic details of oxygen diffusion, despite the lower total oxygen ionic conductivities in the doped compounds presented in this study. Detailed AIMD simulations on

$Bi_{22}W_5O_{48}$ allowed us to obtain a clear picture of the atomic-scale mechanisms, focusing on the similarities and differences to pure δ-Bi_2O_3. Introducing dopants to the structure leads to the localisation and accumulation of oxygen vacancies around the dopant atoms (resulting in the formation of W_4O_{18} tetrahedra of octahedra). This reduces the vacancy concentration (from 25% in pure δ-Bi_2O_3 to 11% in $Bi_{22}W_5O_{48}$) and also the total conductivity. Thorough analysis of coordination numbers as a function of simulation time reveals that W adopts and keeps its octahedral coordination environment. In contrast, Bi coordination fluctuates significantly and Bi atoms adopt a large number of different coordination environments between 5 and 9, with a mean coordination number of 7.4. Analysis of MSDs clearly show that oxygen diffusion is limited to oxygen atoms that are part of the δ-Bi_2O_3 matrix, with highly localised motion (thermal vibrations) of the oxygen atoms that are coordinated to W atoms. This implies that introducing dopants not only reduces the total number of vacancies in the structure (resulting in an increase in oxygen content), but also reduces the number of mobile oxygen atoms from 100% in pure δ-Bi_2O_3 to <60% in $Bi_{22}W_5O_{48}$.

In summary, oxygen diffusion was found to occur almost exclusively in the δ-Bi_2O_3 matrix *via* an isotropic, liquid-like mechanism as observed in pure δ-Bi_2O_3. In contrast to the flexible coordination environments of Bi, transition metal dopant atoms (such as W and Nb) require more regular coordination environments, which localise vacancies and prevent the remaining oxygen atoms from contributing to the overall oxygen diffusivity. This explains the lower overall oxide ionic conductivities. The result demonstrates the utility and potential of the cCE model for quantitative analysis of QENS data, in showing that it can be successfully applied to more complex materials.

Acknowledgments

The authors thank Julia Polt for useful discussions. This work was supported by the Australian Research Council (Discovery Project scheme) and undertaken with the assistance of resources from the National Computational Infrastructure (NCI). J.W. acknowledges financial support from the Australian Institute of Nuclear Science and Engineering (Postgraduate Research Awards scheme).

Author Information

Corresponding Author

* julia.wind@smn.uio.no

Notes

The authors declare no competing financial interests.

References

1. Van Hove, L., Correlations in Space and Time and Born Approximation Scattering in Systems of Interacting Particles. *Phys. Rev.* **1954,** *95* (1), 249-262.
2. Noferini, D.; Koza, M. M.; Rahman, S. M. H.; Evenson, Z.; Nilsen, G. J.; Eriksson, S.; Wildes, A. R.; Karlsson, M., Role of the doping level in localized proton motions in acceptor-doped barium zirconate proton conductors. *Phys. Chem. Chem. Phys.* **2018,** *20* (20), 13697-13704.
3. Noferini, D.; Frick, B.; Koza, M. M.; Karlsson, M., Proton jump diffusion dynamics in hydrated barium zirconates studied by high-resolution neutron backscattering spectroscopy. *J. Mater. Chem. A* **2018,** *6* (17), 7538-7546.
4. Noferini, D.; Koza, M. M.; Karlsson, M., Localized Proton Motions in Acceptor-Doped Barium Zirconates. *J. Phys. Chem. C* **2017,** *121* (13), 7088-7093.
5. Karlsson, M., Proton dynamics in oxides: insight into the mechanics of proton conduction from quasielastic neutron scattering. *Phys. Chem. Chem. Phys.* **2015,** *17* (1), 26-38.
6. Liu, X.; Chen, Y.; Hood, Z. D.; Ma, C.; Yu, S.; Sharafi, A.; Wang, H.; An, K.; Sakamoto, J.; Siegel, D. J.; Cheng, Y.; Jalarvo, N. H.; Chi, M., Elucidating the mobility of H^+ and Li^+ ions in $(Li_{6.25-x}H_xAl_{0.25})La_3Zr_2O_{12}$ *via* correlative neutron and electron spectroscopy. *Energ. Environ. Sci.* **2019,** *12* (3), 945-951.
7. Sacci, R. L.; Lehmann, M. L.; Diallo, S. O.; Cheng, Y. Q.; Daemen, L. L.; Browning, J. F.; Doucet, M.; Dudney, N. J.; Veith, G. M., Lithium Transport in an Amorphous Li_xSi Anode Investigated by Quasi-elastic Neutron Scattering. *J. Phys. Chem. C* **2017,** *121* (21), 11083-11088.
8. Klenk, M. J.; Boeberitz, S. E.; Dai, J.; Jalarvo, N. H.; Peterson, V. K.; Lai, W., Lithium self-diffusion in a model lithium garnet oxide $Li_5La_3Ta_2O_{12}$: A combined quasi-elastic neutron scattering and molecular dynamics study. *Solid State Ionics* **2017,** *312*, 1-7.
9. Nozaki, H.; Harada, M.; Ohta, S.; Watanabe, I.; Miyake, Y.; Ikedo, Y.; Jalarvo, N. H.; Mamontov, E.; Sugiyama, J., Li diffusive behavior of garnet-type oxides studied by muon-spin relaxation and QENS. *Solid State Ionics* **2014,** *262*, 585-588.
10. Willis, T. J.; Porter, D. G.; Voneshen, D. J.; Uthayakumar, S.; Demmel, F.; Gutmann, M. J.; Roger, M.; Refson, K.; Goff, J. P., Diffusion mechanism in the sodium-ion battery material sodium cobaltate. *Sci. Rep* **2018,** *8* (1), 3210.
11. Wind, J.; Mole, R. A.; Yu, D.; Ling, C. D., Liquid-like Ionic Diffusion in Solid Bismuth Oxide Revealed by Coherent Quasielastic Neutron Scattering. *Chem. Mater.* **2017,** *29* (17), 7408-7415.
12. Harwig, H. A.; Gerards, A. G., The polymorphism of bismuth sesquioxide. *Thermochim. Acta* **1979,** *28* (1), 121-131.
13. Harwig, H. A.; Gerards, A. G., Electrical properties of the α, β, γ, and δ phases of bismuth sesquioxide. *J. Solid State Chem.* **1978,** *26* (3), 265-274.
14. Wind, J.; Sharma, N.; Yaremchenko, A. A.; Kharton, V. V.; Blom, D. A.; Vogt, T.; Ling, C. D., Local Structure Adaptations and Oxide Ionic Conductivity in the Type III Stability Region of $(1 - x)Bi_2O_3 \cdot xNb_2O_5$ *Chem. Mater.* **2018,** *30* (10), 3387-3394.
15. Ling, C. D.; Schmid, S.; Blanchard, P. E.; Petricek, V.; McIntyre, G. J.; Sharma, N.; Maljuk, A.; Yaremchenko, A. A.; Kharton, V. V.; Gutmann, M.; Withers, R. L., A (3 + 3)-dimensional "hypercubic" oxide-ionic conductor: type II Bi_2O_3-Nb_2O_5. *J. Am. Ceram. Soc.* **2013,** *135* (17), 6477-84.

16. Wind, J.; Kayser, P.; Zhang, Z.; Radosavljevic Evans, I.; Ling, C. D., Stability and range of the type II $Bi_{1-x}W_xO_{1.5+1.5x}$ solid solution. *Solid State Ionics* **2017,** *308*, 173-180.
17. Wind, J.; Auckett, J. E.; Withers, R. L.; Piltz, R. O.; Maljuk, A.; Ling, C. D., Type II $Bi_{1-x}W_xO_{1.5+1.5x}$: a (3 + 3)-dimensional commensurate modulation that stabilizes the fast-ion conducting delta phase of bismuth oxide. *Acta Cryst. B* **2015,** *71* (Pt 6), 679-87.
18. Wind, J.; Polt, J.; Zhang, Z.; Blom, D. A.; Vogt, T.; Withers, R. L.; Ling, C. D., Rational Design of a Commensurate (3 + 3)-D Modulated Structure within the Fast-Ion Conducting Stabilized δ-Bi_2O_3 Series. *Chem. Mater.* **2017,** *29* (21), 9171-9181.
19. Yu, D.; Mole, R.; Noakes, T.; Kennedy, S.; Robinson, R., Pelican - a Time of Flight Cold Neutron Polarization Analysis Spectrometer at OPAL. *J. Phys. Soc. Jpn.* **2013,** *82* (Suppl.A), SA027.
20. Yu, D.; Mole, R. A.; Kearley, G. J., Performance test on PELICAN – a multi-purpose time of flight cold neutron spectrometer. *EPJ Web of Conferences* **2015,** *83*, 03019.
21. Richard, D.; Ferrand, M.; Kearley, G. J., Analysis and visualisation of neutron-scattering data. *J. Neutron Res.* **1996,** *4* (1), 33-39.
22. Kresse, G.; Furthmüller, J., Efficient iterative schemes forab initiototal-energy calculations using a plane-wave basis set. *Phys. Rev. B* **1996,** *54* (16), 11169-11186.
23. Kresse, G.; Joubert, D., From ultrasoft pseudopotentials to the projector augmented-wave method. *Phys. Rev. B* **1999,** *59* (3), 1758-1775.
24. Perdew, J. P.; Burke, K.; Ernzerhof, M., Generalized Gradient Approximation Made Simple. *Phys. Rev. Lett.* **1996,** *77* (18), 3865-3868.
25. Blöchl, P. E., Projector augmented-wave method. *Phys. Rev. B* **1994,** *50* (24), 17953-17979.
26. Goret, G.; Aoun, B.; Pellegrini, E., MDANSE: An Interactive Analysis Environment for Molecular Dynamics Simulations. *J. Chem. Inf. Model* **2017,** *57* (1), 1-5.
27. Chudley, C. T.; Elliott, R. J., Neutron Scattering from a Liquid on a Jump Diffusion Model. *Proc. Phys. Soc. Lond.* **1961,** *77* (494), 353-&.
28. De Gennes, P. G., Liquid dynamics and inelastic scattering of neutrons. *Physica* **1959,** *25* (7-12), 825-839.
29. Sköld, K., Small Energy Transfer Scattering of Cold Neutrons from Liquid Argon. *Phys. Rev. Lett.* **1967,** *19* (18), 1023-1025.
30. Shannon, R. D., Revised effective ionic radii and systematic studies of interatomic distances in halides and chalcogenides. *Acta Cryst. A* **1976,** *32* (5), 751-767.